



Microstructure and mechanical properties of $\text{Al}_x(\text{TiZrTa}_{0.7}\text{NbMo})$ refractory high-entropy alloys

Zihe Guo ^a, Xiangyang Shen ^a, Feng Liu ^a, Jinyuan Guan ^a, Yue Zhang ^{a,*}, Fuyu Dong ^{a,*}, Yinxiao Wang ^a, Xiaoguang Yuan ^a, Binbin Wang ^b, Liangshun Luo ^b, Yanqing Su ^b, Jun Cheng ^{c,*}

^a School of Materials Science and Engineering, Shenyang University of Technology, Shenyang, China

^b School of Materials Science and Engineering, Harbin Institute of Technology, Harbin, China

^c Northwest Institute for Nonferrous Metal Research, Shaanxi Key Laboratory of Biomedical Metal Materials, Xi'an 710016, China



ARTICLE INFO

Article history:

Received 22 March 2023

Received in revised form 17 May 2023

Accepted 25 May 2023

Available online 26 May 2023

Keywords:

Refractory complex concentrated alloy

Microstructure observation

Strength

Plasticity

Strengthening mechanism

Al content

ABSTRACT

An $\text{Al}_x(\text{TiZrTa}_{0.7}\text{NbMo})$ ($x = 0, 0.1, 0.2, 0.3, 0.4$, and 0.5) series of refractory high-entropy alloys were prepared by a vacuum-arc melting process and annealed. The effects of aluminum (Al) addition on the microstructure, room temperature, and high temperature mechanical properties of refractory high-entropy alloys were systematically examined and the strengthening mechanism analyzed and discussed. The results showed that, the phase composition of the alloy was BCC₁ and BCC₂ phases in the absence of Al. Precipitated phase AlZr₃ formed in the alloy when Al was added. This series of refractory high entropy alloy has good strength at room temperature and high temperature. The compressive yield strength of $\text{Al}_{0.5}(\text{TiZrTa}_{0.7}\text{NbMo})$ alloy at room temperature was 1984 MPa and the compressive yield strength at 800 °C was 714 MPa. All alloys have plastic strain variables of 10.2–34.8 %, showing excellent room temperature plasticity. The increase in yield strength at room temperature primarily resulted from solution and precipitation strengthening. At high temperatures, precipitation strengthening became the dominant strengthening method. These research findings are expected to facilitate the understanding of the influence trends and mechanism of action of Al in refractory high-entropy alloys and serve as a reference for the design and development of Al-containing refractory high-entropy alloys.

© 2023 Elsevier B.V. All rights reserved.

1. Introduction

Metal components are the cornerstone of modern industries, such as aviation, aerospace, automotive manufacturing, and energy production [1]. The strict requirements for metal components determine the material selection and manufacture optimization [2]. The high requirements for material properties in harsh service conditions are most evident in high-temperature alloys. For example, the efficiency of high-pressure turbine engines increases significantly with temperature rise. Thus, the service temperature requirements for high-temperature alloys are becoming increasingly demanding [3]. In recent years, a metallurgical strategy called high-entropy alloys [4,5] has been proposed, which widens the idea for new material design. This novel multi-component alloys have broad

application prospects due to its excellent mechanical properties and high wear resistance and corrosion resistance [6–8]. In a high-entropy alloy system, there is a type of refractory high-entropy alloy (RHEA) composed of high melting point elements, including tungsten, tantalum, molybdenum, niobium, vanadium, and titanium (W, Ta, Mo, Nb, V, and Ti, respectively) [9], which have attracted extensive attention due to its excellent high-temperature mechanical properties. For example, the VNbMoTaW alloy still has a yield strength of 477 MPa at 1600 °C [10], much higher than the service temperature of the conventional high-temperature alloy, Inconel 718. Therefore, refractory high-entropy alloys show high potential and good application prospects for becoming a new generation of high-temperature alloys.

Researchers have tended to examine high-temperature alloys with both low density and high strength. Thus, low-density elements, such as including Al, and Si, are usually used to partially substitute for matrix elements. However, after alloying, the phase composition of refractory high-entropy alloys tends to become more complex. The phase composition includes a multiphase BCC

* Corresponding authors.

E-mail addresses: yuezhang@sut.edu.cn (Y. Zhang), dongfuyu2002@163.com (F. Dong), chengjun_851118@126.com (J. Cheng).

structure changed from an initial single-phase and precipitated phase, such as Laves, M_3Si_5 , Al_xZr_5 , and B2 phases [11–14]. Al is widely used and can be used for room temperature and high temperature strengthening of refractory high-entropy alloys. Senkov [15] et al. have investigated the effects of Al addition on refractory high-entropy alloys $HfNbTaTiZr$ and $CrMo_{0.5}NbTa_{0.5}TiZr$. After alloying with of Al, the hardness and room temperature yield strengths of the above two alloys increases by 29 % and 98 %, respectively, and the high temperature strength increased by 50 % in the temperature range of 800–1200 °C. Qiao [16] et al. have studied the effects of Al element on $Ti_2ZrHf_{0.5}VNb_{0.5}$ alloy and found that the addition of Al not only improves the yield strength of the alloy at room temperature, but also reduces the alloy density and improves the alloy oxidation resistance. Al addition thus has some positive effects on the room temperature, high temperature strength, and oxidation resistance of refractory high-entropy alloys.

However, Al addition can seriously deteriorate room temperature plasticity, regardless of single-phase or multiphase refractory high-entropy alloys. For example, $Al_{0.5}NbTa_{0.8}Ti_{1.5}V_{0.2}Zr$ alloy [17] has a room temperature plasticity of only 4.5 %, which is a typical brittle material. Therefore, in recent years, the brittleness origin of and solution for Al-containing refractory high-entropy alloys have become a new research topic. Soni [18] has conducted a systematic study of $Al_{0.5}NbTa_{0.8}Ti_{1.5}V_{0.2}Zr$ refractory high-entropy alloys and found that B2 phase distributing continuously at grain boundaries is one of the major reasons for the development of room temperature brittleness. Lin [19] has studied the effects of Al addition on $HfNbTaTiZr$ refractory high-entropy alloy and examined that the main cause of the reduction in room temperature plasticity. Plasticity reduction from 50 % to 21 % lay in stress concentration resulting from differences in strength arising from great differences in Al content between branches and dendrites. Now, although there have been many studies and reports on Al-containing refractory high-entropy alloys, many of the trends and mechanisms of actions of Al in the refractory high-entropy alloy system still remain unknown and are expected to be further studied.

Of many refractory high-entropy alloy systems, the $Al-Ti-Zr-Ta-Nb-Mo-V$ alloy system is the most typical one, which is highly dependent on its best room temperature and high temperature yield strengths. For example, the yield strength of $AlTiZrTa_{0.5}NbMo_{0.5}$ alloy can reach 2197 MPa at room temperature, while the yield strength can reach 745 MPa at a high temperature of 1000 °C [20]. This alloy system has become one of the most valuable refractory high-entropy alloy systems due to its excellent mechanical properties [21]. However, the alloy has a room temperature plasticity < 5 % whether subjected to thermal isostatic pressing or annealing treatment. The disadvantage of high brittleness limits the further application of this alloy system. Therefore, it is necessary to continue to optimize the composition of the alloy system to improve plasticity at room temperature. In this study, the composition of $Al_x(TiZr-Ta_{0.7}NbMo)$ was adjusted by Al adjustment of the alloy system ($x = 0, 0.1, 0.2, 0.3, 0.4$, and 0.5), with the alloy fabricated by vacuum arc melting. First, the effects of Al addition on the microstructure and phase composition of the alloy were examined and compared with thermodynamic prediction results (CALPHAD method). Second, the room and high temperature compression properties of $Al_x(TiZr-Ta_{0.7}NbMo)$ alloy were tested to obtain the relationship between strength and plasticity of the designed alloy and the strengthening capacities of Al compared and analyzed. Then, a mechanical model was used to analyze the mechanism of action of Al addition on the strength of these refractory high-entropy alloys. Finally, the related mechanical property data were compared and analyzed with that of current Al-containing refractory high-entropy alloys and their comprehensive mechanical properties evaluated. These research findings will provide some assistance with the development and application of refractory high-entropy alloys.

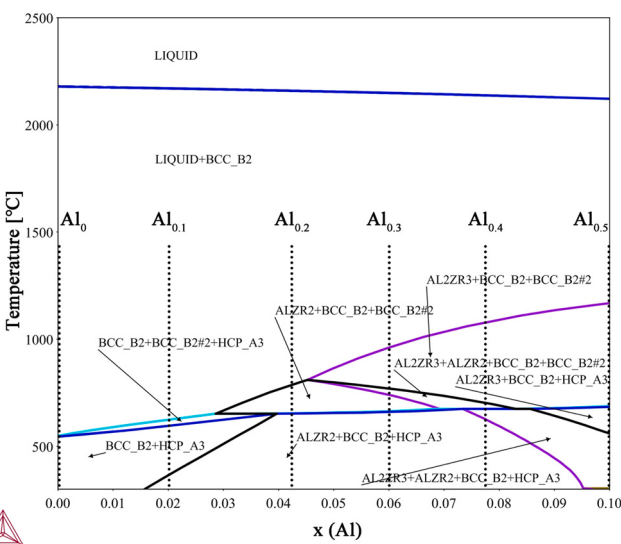


Fig. 1. Pseudo-binary phase diagram of $Al-TiZrTa_{0.7}NbMo$.

2. Experimental procedures

2.1. Alloy design

First, Thermo-calc software (2021 version, TCNI-5 database) was employed to predict the phase composition of this series of refractory high-entropy alloys in the range of temperature between 250 and 2500 °C by means of CALPHAD modeling. A pseudo-binary phase diagram of $Al-TiZrTa_{0.7}NbMo$ showed that, with increased Al content, the types and contents of the precipitated phases dominated by Al-Zr would continue to increase (Fig. 1). Also, the development of a large number of precipitated phases led to a sharp decrease in alloy plasticity, which was inconsistent with the original intention of the alloy design. Therefore, the Al content was specified within 10 at %, that is, ≤ 0.5 mol. In this section, the values of x were set to 0, 0.1, 0.2, 0.3, 0.4, and 0.5, and the corresponding abbreviation of each component was Al_0 , $Al_{0.1}$, $Al_{0.2}$, $Al_{0.3}$, $Al_{0.4}$, and $Al_{0.5}$. Then, the effects of Al addition on the microstructure and mechanical properties of alloy were examined.

2.2. Alloy production and characterization

The raw metals used in the alloys were pure metals with a purity greater than 99.9 %, fabricated by high-vacuum non-self-consumption electric arc furnace after proportional preparation. To prevent oxidation, molten Ti was used to remove oxygen before smelting and high-purity argon (Ar) used as a protective atmosphere during melting. The alloy was repeatedly smelted at a current of 450–500 A to ensure the intensive mixing of alloy components. The button ingots were vacuum-sealed in quartz tubes before they were annealed in a heat treatment furnace. The ingots were annealed at 1000 °C for 12 h before being cooled slowly (10 °C/min).

A Cu-K α monochromatic radiation source was used on a Shimadzu 7000 X-ray diffractometer (XRD; Shimadzu Corp., Kyoto, Japan) for crystal phase identification at a scanning angle of 20–100° and scanning rate of 5°/min. The metallographic samples derived by wire-electrode cutting were sandpaper ground and mechanically polished before being subjected to metallographic corrosion by aqua regia. Microstructural observation and compositional analysis were conducted on the alloy using a scanning electron microscope (SEM; FEI Q45, FEI Co., Hillsboro, OR, USA) equipped with X-ray energy dispersive spectrometer (EDS). To ensure accurate results, 5 different locations were selected for observation. Transmitted samples of

$\Phi 3 \times 0.5$ mm derived from wire cutting were ground to 50 μm before being thinned using an ion thinning meter (Gatan 691, Ametek, Inc., Berwyn, PA, USA). The prepared transmission sample was put in a transmission electron microscope (TEM; Tecnai G2 F20, FEI Co.) for microscopic tissue observation. Image J image processing software was used to analyze the precipitated phase size and volume fraction in TEM photos. When compressed at room temperature, a cylindrical specimen with a size of $\Phi 3 \times 6$ mm was placed on a WDW-100 electronic universal testing machine at a strain rate of $5 \times 10^{-4} \text{ s}^{-1}$ for compression testing. To ensure the accuracy of experimental results, the room temperature compression experiments for each component alloy were repeated 3 times. A Gleeble 3500 thermal simulation testing machine (Dynamics Systems, Inc., Poestenkill, NY, USA) was used for high-temperature compression experiments. In the experiment, high-purity Ar was introduced as a protective atmosphere and temperatures measured with a platinum-rhodium (Pt-Rh) thermocouple. The sample was separated from the indenter by a Ta sheet, with graphite as a lubricant and it was assured that an uniform force was applied. The sample size was $\Phi 6 \times 9$ mm. At a strain rate of $1 \times 10^{-3} \text{ s}^{-1}$, high temperature compression experiments were performed at 800, 1000, and 1200 °C. Upon completion of the experiment, the specimen was put into water and quenched to retain the high-temperature deformed structure. To ensure the accuracy of experimental results, high-temperature compression experiments were repeated 3 times under each condition.

3. Results

3.1. XRD analysis and phase identification

XRD patterns of the $\text{Al}_x(\text{TiZrTa}_{0.7}\text{NbMo})$ ($x = 0, 0.1, 0.2, 0.3, 0.4$, and 0.5) series of annealed alloys indicated that, in the absence of Al, all diffraction peaks in the XRD curve showed that the Al_0 alloy phase was a BCC structure (Fig. 2). The presence of peaks on diffraction patterns, such as (110) and (211), indicated that the alloys contained two BCC phases (BCC_1 and BCC_2). According to the Bragg diffraction equation, the lattice constants of the two were 0.3314 and 0.3383 nm, respectively. When Al was added, peak splitting was still observed on the diffraction peak, indicating that Al addition did not significantly affect the phase structure of the solid solution in the

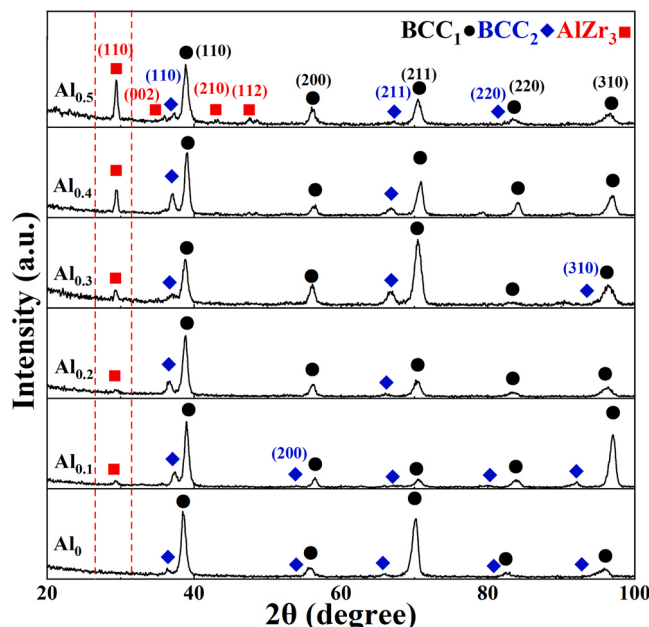


Fig. 2. XRD patterns of $\text{Al}_x(\text{TiZrTa}_{0.7}\text{NbMo})$ alloys after annealing.

alloy. As Al content increased, some new diffraction peaks occurred in the XRD patterns, especially when the Al content was up to 0.5 mol. Based on an analysis using software Jade 5.0, these diffraction peaks corresponded to the AlZr_3 phase, an L_1_2 precipitated phase. In addition, as shown by the red-dotted area in Fig. 2, the intensity of the (110) diffraction peak increased significantly with increased Al content, indicating that the precipitated phase containing Al was increasing.

3.2. Microstructure characterization

The microstructure of annealed $\text{Al}_x(\text{TiZrTa}_{0.7}\text{NbMo})$ alloy showed that the Al_0 alloy formed a microstructure primarily composed of dendrite (BCC_1 phase) and intergranular region (BCC_2 phase) due to the high component subcooling caused by the multicomponent characteristics of high-entropy alloys (Fig. 3a). After Al addition, the branch part did not change significantly and the formation of fine precipitated phases found between the dendrites. The volume of the precipitated phase at the BCC_1 phase boundary increased (Fig. 3b–3e), especially when Al increased to 0.5 mol (Fig. 3f).

The SEM-EDS surface distributions of each element in $\text{Al}_x(\text{TiZrTa}_{0.7}\text{NbMo})$ alloys showed that, according to the distribution of the element surface, Ta, Mo, and Nb in the alloy were clearly mainly distributed in the branch parts, while Al, Ti, and Zr were distributed in the dendrites. The separation between Ta-Zr was the most clear. From a thermodynamic point of view, this was because the binary mixing enthalpies $\Delta H_{\text{Ta}-\text{Ti}}$, $\Delta H_{\text{Ta}-\text{Zr}}$, $\Delta H_{\text{Nb}-\text{Ti}}$, and $\Delta H_{\text{Nb}-\text{Zr}}$ are all positive values [22], such that Ti and Zr were discharged from the main dendrite phases (Ta and Mo) with high melting points. At the same time, Al, Ti and Zr were concentrated in the dendrites due to the low mixing enthalpies of the three. In addition, according to the Ta-Zr binary phase diagram [23], the Ta-Zr binary alloy would undergo phase separation at 1747 °C, forming a Ta and Zr-rich bi- β phase, resulting in separation between Ta and Zr. Fig. 4.

In SEM-EDS point analysis results of micro-area chemical composition in $\text{Al}_x(\text{TiZrTa}_{0.7}\text{NbMo})$ alloys (Table 1), C_{da} represents the branch region, C_{idr} the interdendrite region, and C_{aver} the average composition. The micro-area chemical composition of the alloy can show the segregation of components of nonequilibrium solidification. At the same time, the melting point of the components in the alloy determined the order of element precipitation in the non-equilibrium solidification process. Hence, linking the two allows the analysis of the degree of microscopic segregation in the alloys. Senkov [9] et al. have found a linear relationship $\Delta C = k\Delta T$ between parameter $\Delta C = C_{da} - C_{aver}$ and parameter $\Delta T = T_i - T_m$ when studying the relationship between composition segregation and alloy melting point. However, this relationship does not apply to refractory high-entropy alloys with nonequal molar ratios. For this reason, Ge [24] has changed ΔC to $\delta C = (C_{da} - C_{aver})/C_{aver}$, but this would cause the scale factor k to deviate. Therefore, based on research findings obtained by Ge et al., two new parameters were proposed here, expressed as

$$\delta C = (C_{da} - C_{aver})/C_{aver} \quad (1)$$

$$\delta T = (T_i - T_m)/T_m \quad (2)$$

where, T_i represents the melting point of element i and T_m the theoretical melting point of the alloy, calculated by the law of mixtures. The δC in Eq. 1 could be used as a measure of elemental component segregation. If all elements were evenly distributed, then $\delta C = 0$. A larger absolute value of δC indicated a greater degree of segregation of an element. Similarly, δT could be used as a measure of the order in which elements were precipitated. If all elements had the same melting point, then $\delta T = 0$. A greater δT indicated a higher precipitation order of elements during solidification. A larger scale factor k indicated a greater degree of alloy segregation [25]. Based on

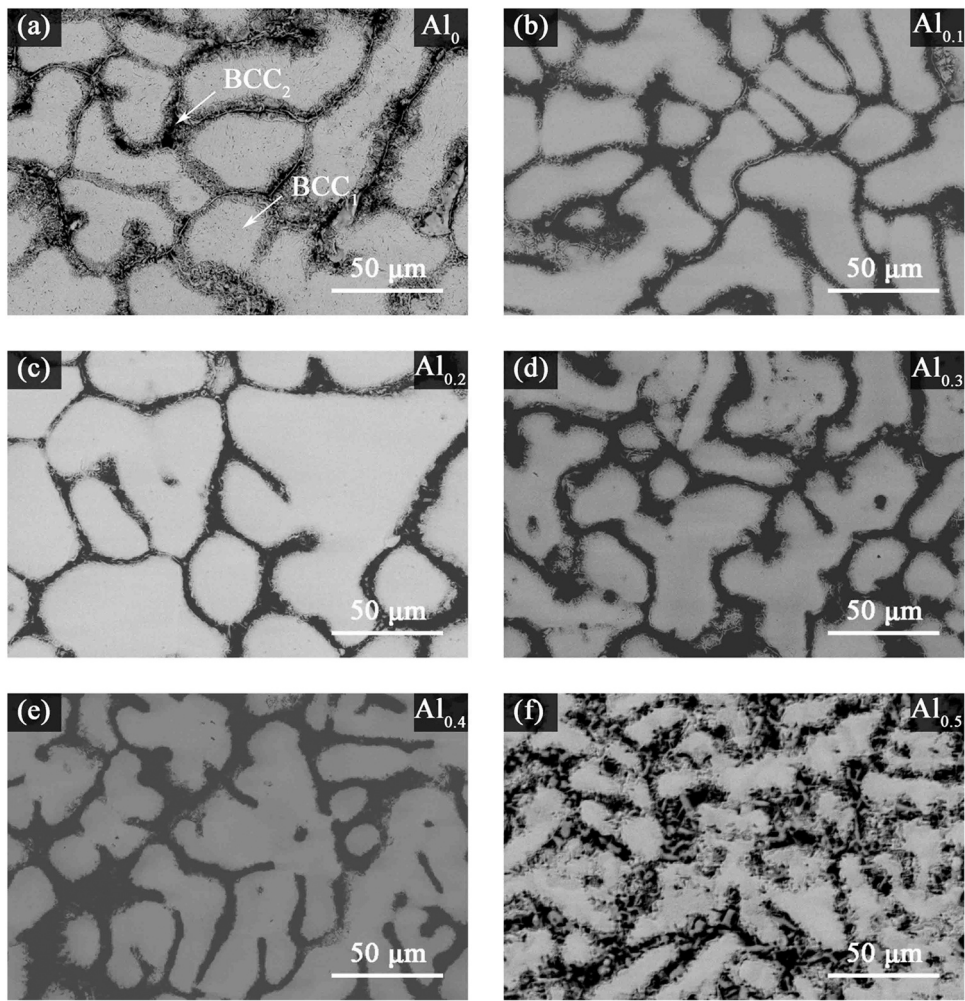


Fig. 3. SEM-BSE images of $\text{Al}_x(\text{TiZrTa}_{0.7}\text{NbMo})$ alloys after annealing: Al_0 , $\text{Al}_{0.1}$, $\text{Al}_{0.2}$, $\text{Al}_{0.3}$, $\text{Al}_{0.4}$, and $\text{Al}_{0.5}$ (a–f, respectively).

the melting points of the elements and the data in Table 1, the relationship between δC and δT was obtained (Fig. 5). Ta, Mo, and Nb were distributed in the first quadrant, indicating that these high melting point elements were preferentially precipitated during solidification. Al, Ti, and Zr were in the third quadrant, suggesting that they are segregated elements in the final stage of solidification, chiefly distributed in the dendrites. These points were linearly fitted to derive the dotted line in the graph. With increased Al content, the slope of the fitted line became higher, indicating that Al addition increased the segregation degree of elements in the alloy.

Bright field (BF) images of Al_0 high-entropy alloy TEM and the corresponding selective electron diffraction pattern showed that the microscopic topography of the alloy possessed characteristics similar to that of dendrites in Fig. 3 (Fig. 6a). Based on the selected electron diffraction patterns (Fig. 6c and 6d), the two were phases BCC_1 and BCC_2 , respectively, which coincided with the XRD analysis in Fig. 2. Dark field (DF) images allowed clear observation of the position relationship between the two phases (Fig. 6b). The dendrite part was BCC_1 phase and the intergranular part BCC_2 phase.

TEM characterization of $\text{Al}_{0.1}$ and $\text{Al}_{0.5}$ alloys showed that, after Al addition, there was no pronounced change in the morphology of BCC_1 and BCC_2 phases in the matrix (Fig. 7). However, the generation of spherical precipitated phases was observed due to the fact that Al was prone to reaction with Zr in BCC_2 phase. In $\text{Al}_{0.5}$ alloy, more spherical precipitated phases were clearly observed due to increased added Al (Fig. 7d). Based on an analysis of the corresponding

selected-area diffraction pattern, the precipitated phase was AlZr_3 phase.

3.3. Mechanical properties

Next, the $\text{Al}_x(\text{TiZrTa}_{0.7}\text{NbMo})$ series of alloys were tested for compression properties at room and high temperature. The room temperature compressive stress-strain curve and relevant mechanical properties are shown in Fig. 8a and Table 2. When Al was not added, the room temperature plasticity of Al_0 alloy was 34.8 %, but the yield strength was low. After Al addition, the yield strength increased, while the Young's modulus of the alloy also increased. The relationship between yield strength and plastic strain of high-entropy alloy was observed and the strength found to increase while the plasticity decreased (Fig. 8b). In addition, yield strength and plastic strain appeared to have a linear relationship with Al content. For each 0.1 mol increase in Al content, the yield strength increased by 127 MPa and plastic strain decreased by 4.92 %. When Al content increased to 0.5 mol, the plastic strain of the material was reduced to 10.2 %, indicating that the addition of excess Al worsened plasticity at room temperature. The reasons for the increase in yield strength of materials will be discussed in detail in Section 4.2.

High-temperature compressive stress-strain curves of $\text{Al}_x(\text{TiZrTa}_{0.7}\text{NbMo})$ series alloys are shown in Fig. 9 and the relevant high-temperature mechanical properties in Table 3. For alloys of the same composition, the yield strength decreased with temperature rise. After Al addition, the degree of reduction of alloy yield strength

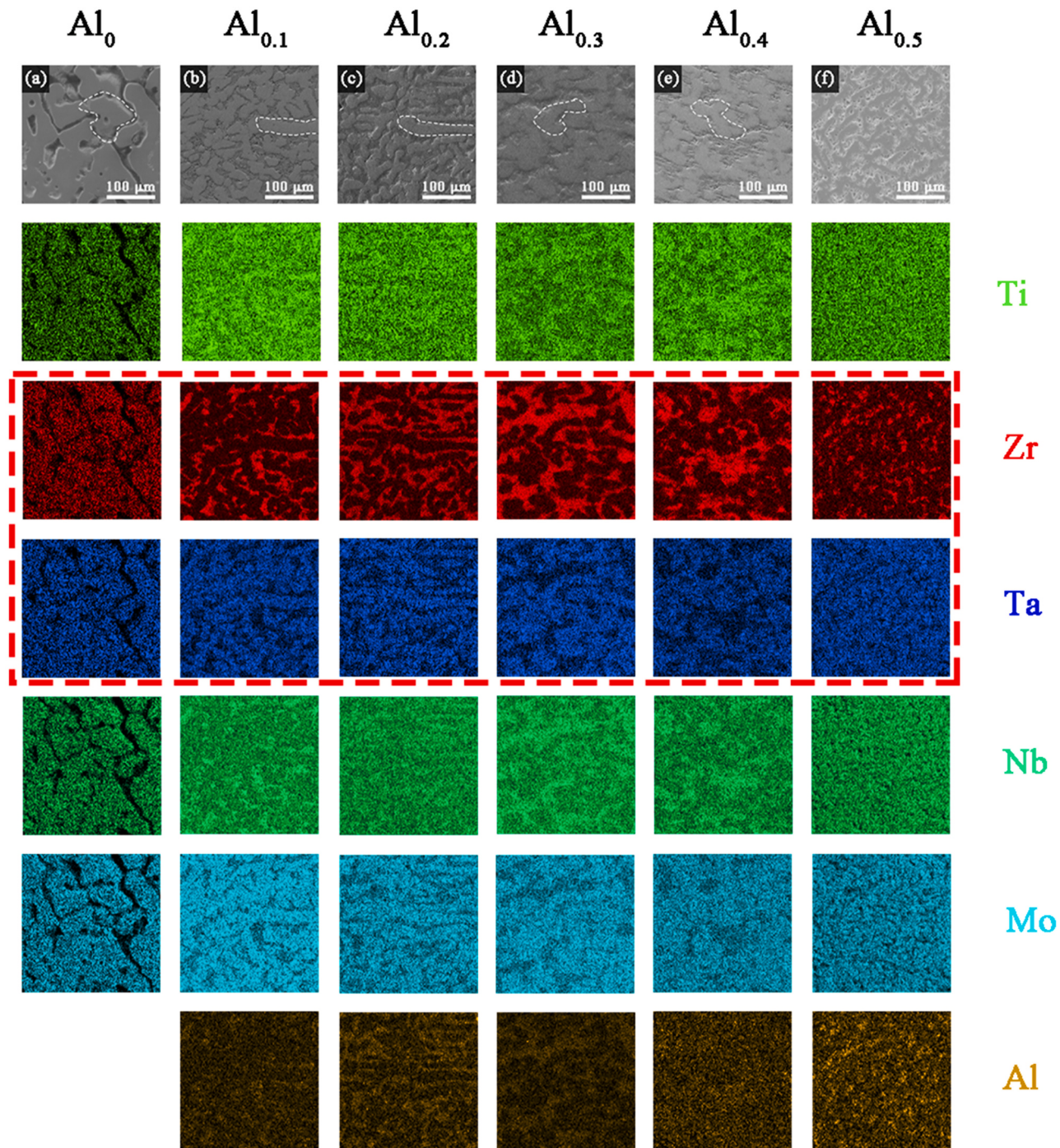


Fig. 4. Energy dispersive spectrometer (EDS) mappings of $\text{Al}_x(\text{TiZrTa}_{0.7}\text{NbMo})$ alloys: Al_0 , $\text{Al}_{0.1}$, $\text{Al}_{0.2}$, $\text{Al}_{0.3}$, $\text{Al}_{0.4}$, and $\text{Al}_{0.5}$ (a–f, respectively).

caused by temperature rise was lower than that in the absence of Al. According to the ratio of yield strength at 1200–800 °C in Table 3, When the compression temperature is 800 °C and the content of Al element is 0.5 mol, the alloy has the highest yield strength and the influence of temperature is the least. When the compression temperature increased to 1200 °C, the yield strengths of all alloys were reduced to a range between 113 and 150 MPa.

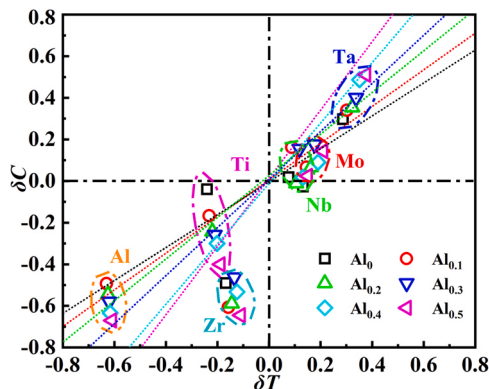
3.4. Microstructures after high temperature compression

SEM observations were performed on the thermocompression microstructure at a compression temperature of 1200 °C (Fig. 10). The loading direction was the vertical axis (Fig. 10a, white arrow). To

prevent the effects of the indenter restraint effect, all material observation photographs were derived from the deformed sample core. In high-temperature rheological structures without Al, the branch region (BCC₁ phase), where Ta, Mo, and Nb were enriched, were clearly distinguished from the intergranular region (BCC₂ phase), where Ti, Zr, and Al elements were enriched (Fig. 10a). Under the action of external stress, some short rod-shaped BCC₁ phases began to experience plastic deformation in a direction perpendicular to loading, while BCC₂ phases experienced plastic deformation along BCC₁ phases. The high-temperature rheological structure after Al addition showed that, before thermal deformation, combination reactions between Al and intergranular Zr led to generation of the precipitated phase (Fig. 10b–10f). Therefore, a large number of grains

Table 1Chemical compositions (wt %) of $\text{Al}_x(\text{TiZrTa}_{0.7}\text{NbMo})$ alloys after annealing.

Alloys	Ti	Zr	Ta	Nb	Mo	Al
Al_0	C_{da}	8.41	7.89	45.47	17.04	21.19
	C_{idr}	7.60	18.25	16.70	19.18	38.27
	C_{aver}	7.61	11.58	25.97	18.56	36.28
$\text{Al}_{0.1}$	C_{da}	8.37	10.50	37.23	22.86	20.86
	C_{idr}	13.30	41.41	14.27	18.53	11.71
	C_{aver}	11.95	26.73	24.64	19.68	16.46
$\text{Al}_{0.2}$	C_{da}	7.72	6.67	45.12	18.79	21.40
	C_{idr}	13.99	30.56	10.54	19.89	23.21
	C_{aver}	10.40	16.21	31.67	18.99	22.07
$\text{Al}_{0.3}$	C_{da}	8.25	20.15	31.68	20.63	18.88
	C_{idr}	6.31	68.38	7.84	9.37	7.10
	C_{aver}	7.59	37.50	24.13	16.44	13.72
$\text{Al}_{0.4}$	C_{da}	7.97	7.68	38.95	23.97	20.72
	C_{idr}	11.81	36.26	16.26	20.59	12.10
	C_{aver}	9.57	16.46	30.02	23.55	19.01
$\text{Al}_{0.5}$	C_{da}	6.99	6.17	43.53	20.22	22.29
	C_{idr}	12.90	36.33	15.11	18.83	12.63
	C_{aver}	9.24	17.39	32.21	19.74	19.49
						1.93

**Fig. 5.** Correlation between δC and δT .

were produced in the BCC_2 phase after thermal deformation. Due to the action of external stress, the BCC_2 phase containing the precipitated phase underwent more severe deformation, resulting in a finer and more uniform structure.

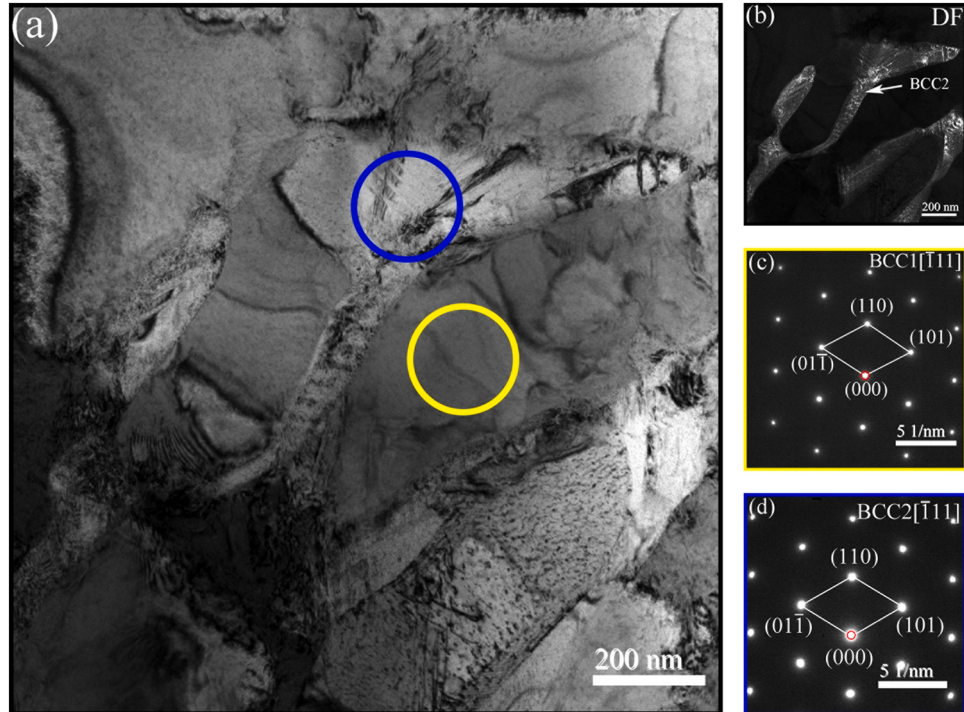
4. Discussion

4.1. Equilibrium phase diagrams

The phase composition of high-entropy alloys are generally judged by semi-empirical criteria (mixed entropy, mixed enthalpy, and valence electron concentration) [26,27]. However, due to Al addition in this alloy system, the above criterion equation no longer applied [28]. Therefore, it was a good option to analyze the phase composition of high-entropy alloys using CALPHAD modeling. The prediction results of the equilibrium phase diagrams of Al_0 , $\text{Al}_{0.1}$, and $\text{Al}_{0.5}$, are shown in Fig. 11a–11c, respectively.

According to the thermodynamic phase diagram analysis during the solidification process of alloy Al_0 , phase BCC_1 was first precipitated at ~ 2270 °C, phase BCC_2 precipitated at 1250 °C, and $\text{BCC}_2 \rightarrow \text{HCP}$ phase transition at 700 °C (Fig. 11a). When 0.1 mol of Al was added, there was no significant change in the phase composition of alloy $\text{Al}_{0.1}$ (Fig. 11b). However, the precipitation temperature of BCC_2 phase rose significantly and content also increased somewhat. For alloy $\text{Al}_{0.5}$, due to increased Al, the alloy produced phase Al_2Zr_3 at 1200 °C and phase AlZr_2 at 600 °C (Fig. 11b). The content of phase BCC_1 also decreased somewhat. The final phase composition of the alloy was 55 % BCC_1 phase, 24 % HCP phase, 10 % AlZr_2 , and 11 % Al_2Zr_3 .

Based on the actual phase composition of the alloy, the thermodynamic model successfully predicted that the alloy was composed of phases BCC_1 and BCC_2 . However, there were two discrepancies in the phase diagram (Fig. 11). On one hand, under actual conditions, the $\text{BCC}_2 \rightarrow \text{HCP}$ phase transition, as shown in the phase diagram, did not occur in the alloy at 700 °C. This was because the thermal stability of the HCP phase was much lower than that of

**Fig. 6.** TEM images and corresponding SAED patterns of Al_0 alloy after annealing. TEM BF images of Al_0 alloy and TEM DF image in the same position (a and b, respectively) and SAED patterns of BCC_1 and BCC_2 (c and d, respectively).

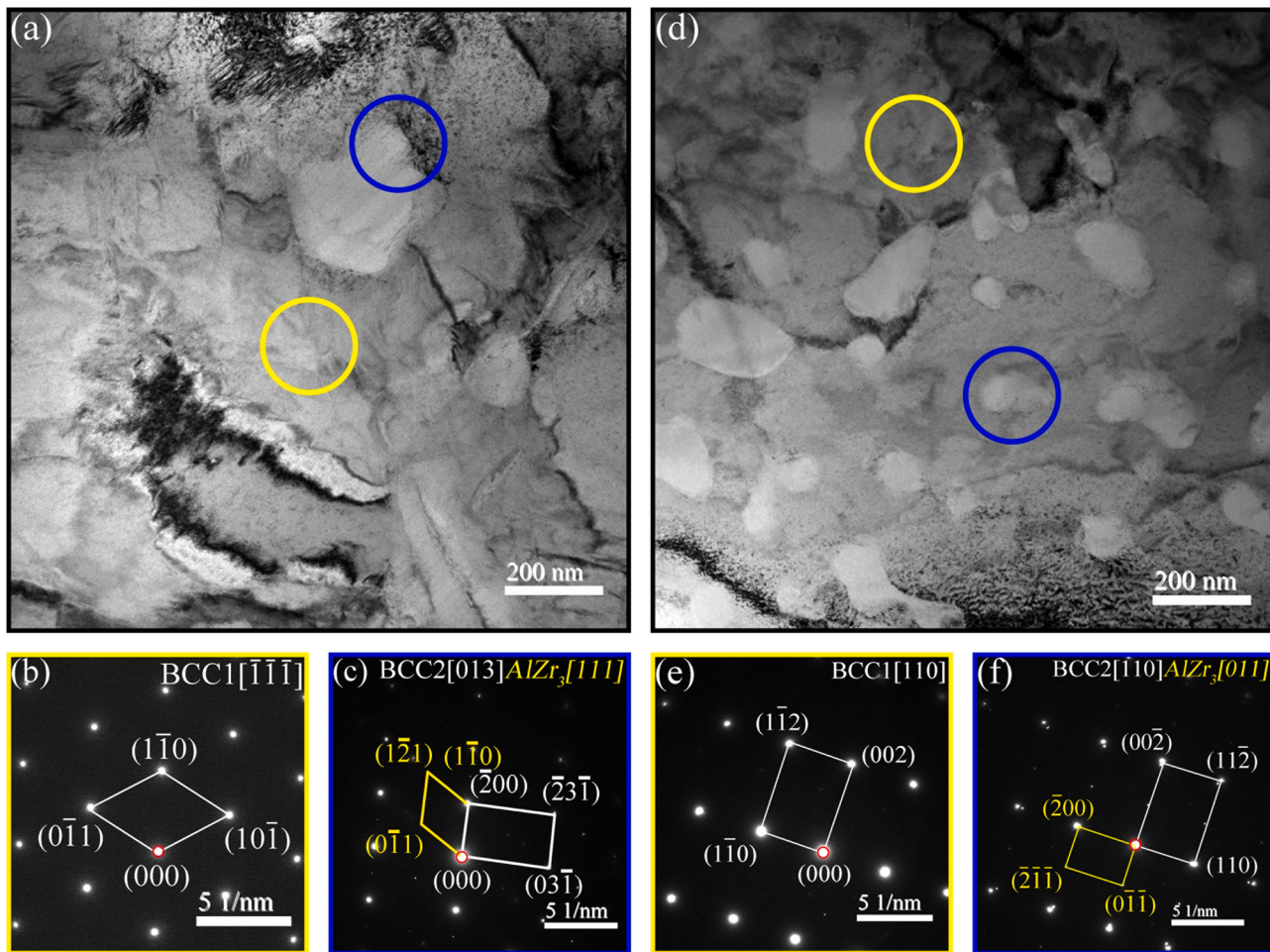


Fig. 7. TEM images and corresponding SAED patterns of Al_{0.1} and Al_{0.5} alloy after annealing. TEM BF images of Al_{0.1} and Al_{0.5} alloy (a and d, respectively) and SAED patterns of BCC₁ and BCC₂ in Al_{0.1} and Al_{0.5} alloys (b & c and e & f, respectively).

the BCC phase [29]. In addition, as the alloy ingots prepared by arc melting cooled down quickly and sufficient time was not provided for atomic diffusion, the BCC₂→HCP phase transition was less likely to occur during the cooling process [30]. In addition, only the AlZr₃ phase was detected in Al_{0.5} alloy, but Al₂Zr₃ and AlZr₂ phases present in the phase diagram were not detected. This might have been associated with the subsequent annealing treatment.

4.2. Room temperature strengthening mechanism

In general, the increase in yield strength of metal materials at room temperature was associated with many factors, such as grain boundary strengthening [31], solution strengthening [32], and work hardening [33]. The high yield strength of high-entropy alloys is largely attributable to solution strengthening [34]. Of course, if there

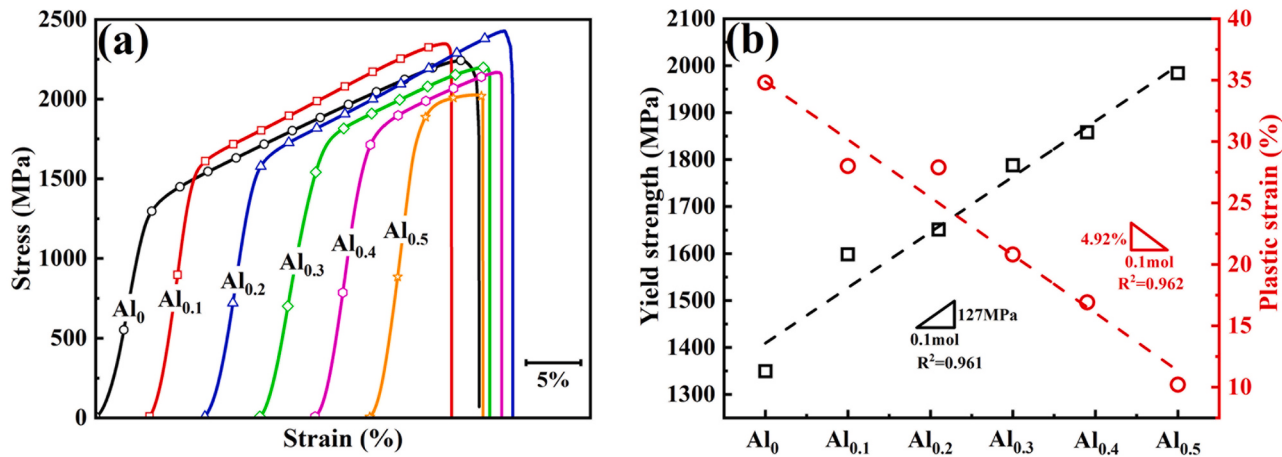


Fig. 8. Compressive stress-strain curves of Al_x(TiZrTa_{0.7}NbMo) alloys tested at room temperature (a) and effect of Al molar content on yield strength and plastic strain of Al_x(TiZrTa_{0.7}NbMo) alloys (b).

Table 2

Room temperature compression properties (Young's modulus, E , yield stress, σ_y , fracture stress, σ_f , elastic strain, ε_e , and plastic strain, ε_p) of the $\text{Al}_x(\text{TiZrTa}_{0.7}\text{NbMo})$ alloys.

Properties	Alloys					
	Al_0	$\text{Al}_{0.1}$	$\text{Al}_{0.2}$	$\text{Al}_{0.3}$	$\text{Al}_{0.4}$	$\text{Al}_{0.5}$
σ_y (MPa)	1349 ± 20	1598 ± 20	1651 ± 15	1788 ± 10	1858 ± 15	1984 ± 10
σ_f (MPa)	2242	2349	2427	2198	2165	2062
E (GPa)	105 ± 4	112 ± 3	121 ± 3	133 ± 4	145 ± 4	163 ± 5
ε_e (%)	4.3	3.6	4.3	5	3.7	3.54
ε_p (%)	34.8	28	27.9	20.8	16.9	10.2

is a precipitation phase in the alloy, precipitation strengthening might also occur. Also, this might lead to competition between strengthening mechanisms. In this study, the precipitation phase was formed due to Al addition, which significantly elevated alloy yield strength. Therefore, the degree of contribution made by both solid solution and precipitation strengthening was analyzed and discussed.

It is well known that the precipitation strengthening mechanism of metals can be divided into dislocation cutting and bypassing mechanisms [35]. Research by Li et al. [36] has shown that the strengthening of the precipitated phase generation in refractory high-entropy alloys is dominated by the shear mechanism. In addition, based on the TEM analysis above, as L1_2 -type AlZr_3 precipitated in the designed alloy had a large number of drivable-slip systems [37], it had excellent room temperature plasticity. In summary, the precipitation strengthening mode of the alloy designed here might be deemed as a dislocation cutting mechanism. As no subsequent deformation treatment was carried out in this study, there were no effects from dislocation and grain boundary strengthening. Therefore, the yield strength expression formula of the alloy here was

$$\sigma_y = \sigma_A + \Delta\sigma_{ss} + \Delta\sigma_p \quad (3)$$

where σ_A is the intrinsic lattice frictional resistance, calculated by the mixture rule. Regarding the solid solution strengthening effect

Table 3

Mechanical properties of $\text{Al}_x(\text{TiZrTa}_{0.7}\text{NbMo})$ alloys at high temperatures obtained via compressive stress-strain curves.

Properties	Alloys					
	Al_0	$\text{Al}_{0.1}$	$\text{Al}_{0.2}$	$\text{Al}_{0.3}$	$\text{Al}_{0.4}$	$\text{Al}_{0.5}$
σ_y (MPa) at 800 °C	518	522	550	563	571	714
σ_y (MPa) at 1000 °C	342	350	445	460	473	495
σ_y (MPa) at 1200 °C	113	125	139	141	147	150
$\sigma_y^{1200^\circ\text{C}}/\sigma_y^{800^\circ\text{C}}$	0.218	0.239	0.252	0.250	0.257	0.210

($\Delta\sigma_{ss}$), based on research by Labusch [38] and Wang [39] et al., its contribution value was

$$\Delta\sigma_{ss} = \frac{G}{45} (\sum_i \varepsilon_i X_i)^{2/3}, \quad (4)$$

where, G is the shear modulus of the alloy, calculated by the mixture rule; X_i the atomic percentage of element i , and ε_i the mismatch factor, which was expressed as

$$\varepsilon_i = \sqrt{\eta_i^2 + \alpha^2 \delta_i^2} \text{ and} \quad (5)$$

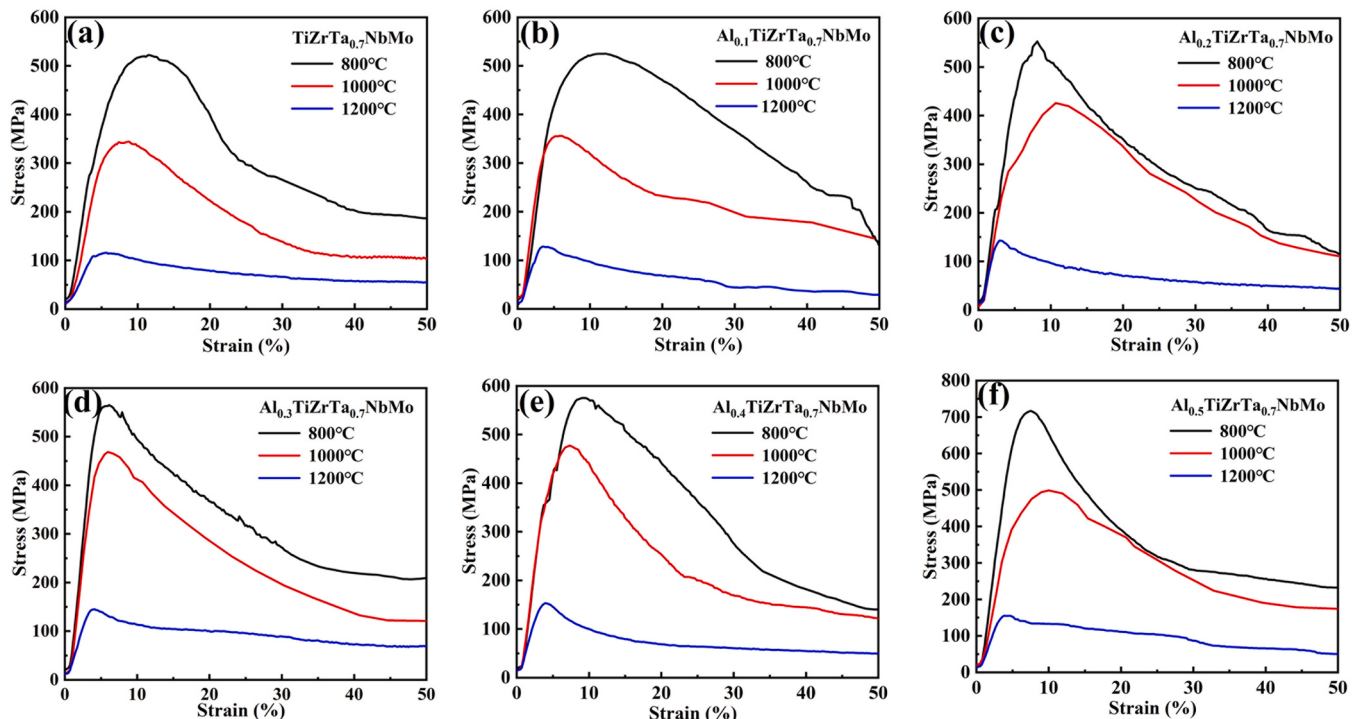


Fig. 9. Compressive stress-strain curves of $\text{Al}_x(\text{TiZrTa}_{0.7}\text{NbMo})$ at high temperatures: Al_0 , $\text{Al}_{0.1}$, $\text{Al}_{0.2}$, $\text{Al}_{0.3}$, $\text{Al}_{0.4}$, and $\text{Al}_{0.5}$ (a-f, respectively).

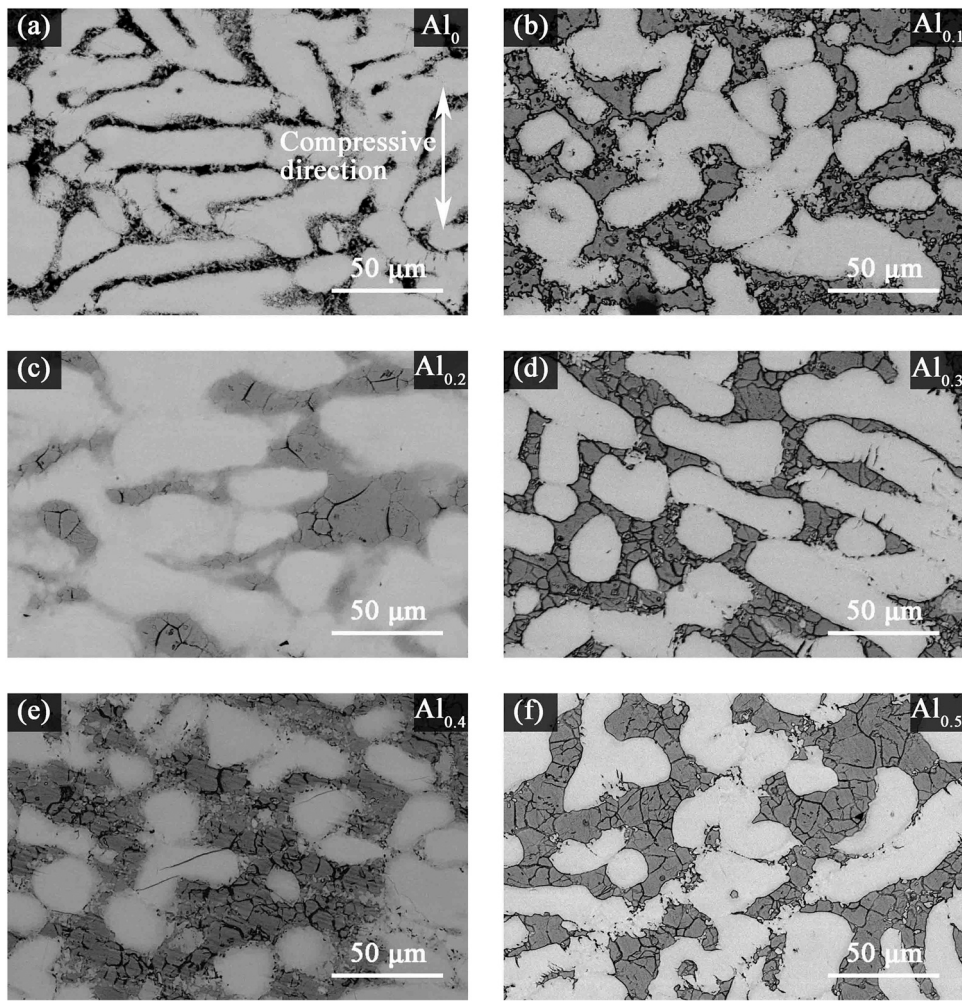


Fig. 10. Microstructures of the $\text{Al}_x(\text{TiZrTa}_{0.7}\text{NbMo})$ alloys after compression testing at 1200 °C: Al_0 , $\text{Al}_{0.1}$, $\text{Al}_{0.2}$, $\text{Al}_{0.3}$, $\text{Al}_{0.4}$, and $\text{Al}_{0.5}$ (a-f, respectively).

$$\eta'_i = \frac{\eta_i}{1 + \left| \frac{\eta_i}{2} \right|}, \quad (6)$$

where α is a physical constant related to dislocation, generally assigned 16 [40] in high-entropy alloys; η'_i the shear modulus mismatch parameter; δ_i the atomic radius mismatch parameter. The expression for the shear modulus mismatch parameter and the atomic radius mismatch parameter presented by Senkov [41] et al. was

$$\eta_i = \frac{9}{8} \sum X_j \eta_{ij} \text{ and} \quad (7)$$

$$\delta_i = \frac{9}{8} \sum X_j \delta_{ij}, \quad (8)$$

where, the expressions of η_{ij} and δ_{ij} were

$$\eta_{ij} = 2 \frac{G_i - G_j}{G_i + G_j} \text{ and} \quad (9)$$

$$\delta_{ij} = 2 \frac{r_i - r_j}{r_i + r_j}, \quad (10)$$

where, G_i and G_j represent the shear modulus of the elements i and j , respectively, and r_i and r_j the atomic radii of the elements i and j , respectively. After consulting the literature, the physical parameters

of the relevant pure elements [39,42,43] are summarized in Table 4. At this time, the contributions to solution strengthening of Al_0 , $\text{Al}_{0.1}$, and $\text{Al}_{0.5}$ alloys were calculated quantitatively, with the calculated results at 267 MPa, 261.61 MPa and 244 MPa, respectively.

The precipitation strengthening effect ($\Delta\sigma_p$) is primarily derived from the effects of coherent ($\Delta\sigma_{CS}$), modulus ($\Delta\sigma_{MS}$), and order ($\Delta\sigma_{OS}$) strengthenings. In the shear mechanism, coherent and modulus strengthenings occur before the shear process, while order strengthening occurred after the shear process. The greater of $\Delta\sigma_{CS} + \Delta\sigma_{MS}$ and $\Delta\sigma_{OS}$ will dominate the shear process. Their expressions [44–47] were expressed as

$$\Delta\sigma_{CS} = M \cdot \alpha_e (G \cdot \varepsilon)^{3/2} \left(\frac{rf}{0.5Gb} \right)^{1/2}, \quad (11)$$

$$\Delta\sigma_{MS} = 0.0055 \cdot M \Delta G^{3/2} \left(\frac{2f}{G} \right)^{1/2} \left(\frac{r}{b} \right)^{3m/2-1}, \text{ and} \quad (12)$$

$$\Delta\sigma_{OS} = M \cdot 0.81 \frac{\gamma_{apb}}{2b} \left(\frac{3\pi f}{8} \right)^{1/2}, \quad (13)$$

where, M is the Taylor factor, which is the coefficient when the shear modulus is converted from and to the normal modulus, with the value usually 2.73 for BCC-type alloys; α_e is constant, at 2.6 [48]; G the shear modulus of the alloy, which can be calculated from $G = E/(2(1 + \nu))$; E obtained by compression testing; and ν the

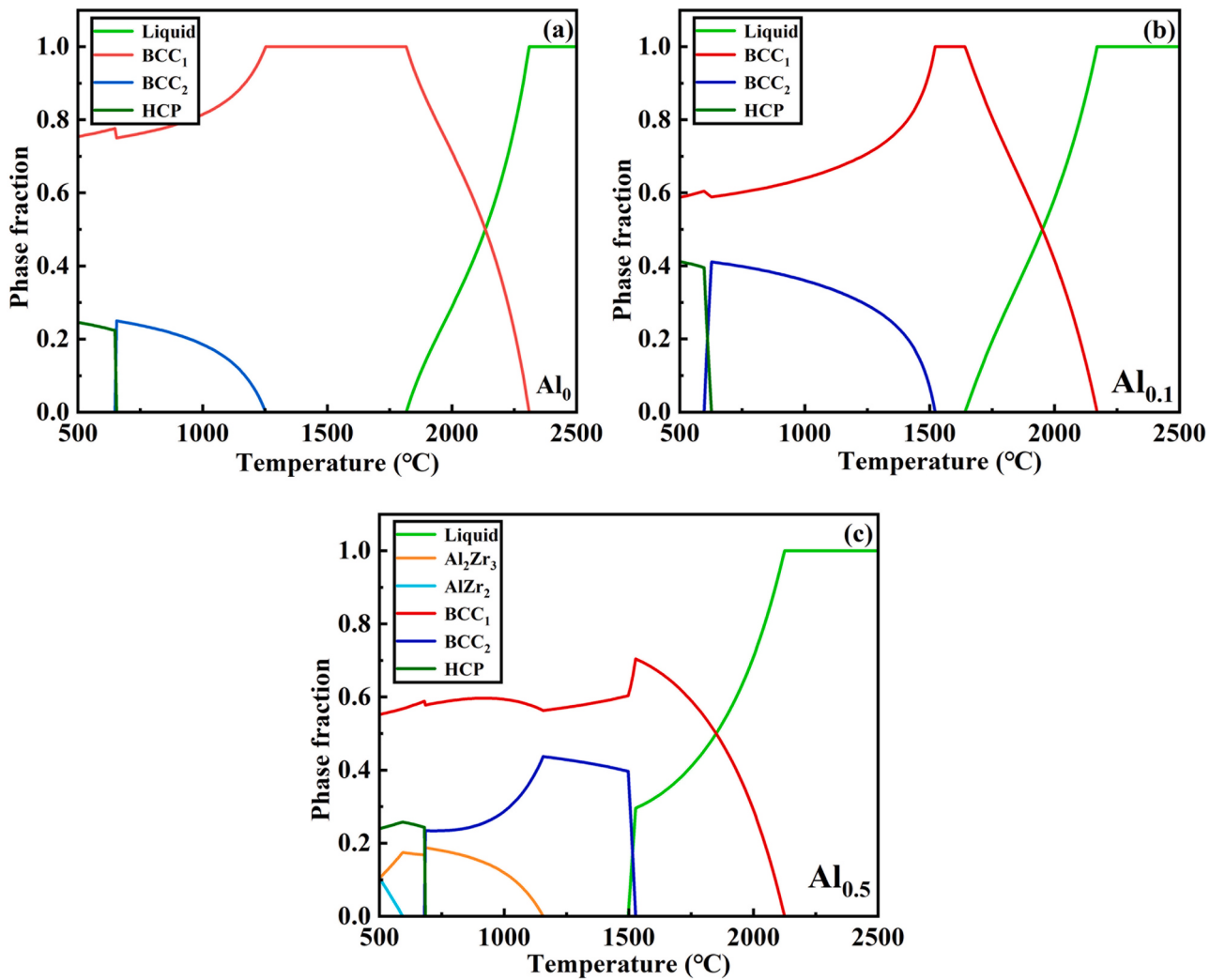


Fig. 11. Calculated equilibrium phase diagrams for Al_0 , $\text{Al}_{0.1}$, and $\text{Al}_{0.5}$ (a–c, respectively).

Table 4

Atomic radius r , shear modulus G , and yield strength σ_y of the relevant refractory metal elements at room temperature from Ref. [39,42,43].

Properties	Elements					
	Ti	Zr	Ta	Nb	Mo	Al
r (pm)	141.8	155.1	143.0	142.9	136.3	143
G (GPa)	45.6	35	69.2	37.5	125.6	25
σ_y (MPa)	195	280	170	240	420	30

Table 5

Data used for the strength calculations of $\text{Al}_{0.1}$ and $\text{Al}_{0.5}$, including matrix shear modulus (G), shear modulus difference between matrix and precipitates (ΔG), lattice misfits (ϵ), the volume fraction (f) of precipitates, burger's vector (b), particle size (r) of precipitates.

Alloys	G (GPa)	ΔG (GPa)	ϵ (%)	f (%)	b (nm)	r (nm)
$\text{Al}_{0.1}$	43.07	12.07	0.28	1	0.283	140
$\text{Al}_{0.5}$	63	7.86	0.27	10	0.284	145

Table 6

Strength contributions during solution strengthening and shearing process.

Alloys	σ_A (MPa)	$\Delta\sigma_{ss}$ (MPa)	$\Delta\sigma_{CS}$ (MPa)	$\Delta\sigma_{MS}$ (MPa)	$\Delta\sigma_{OS}$ (MPa)
Al_0	267	1119	0	0	0
$\text{Al}_{0.1}$	261.61	1092	142	75	190
$\text{Al}_{0.5}$	244	1014	634	104	697

Poisson's ratio. Unfortunately, a Poisson's ratio for this component system could not be found. However, research by Gao [11] et al. has shown that, when the Poisson's ratio of refractory high-entropy alloy is 0.3, the alloy mechanical properties can be well predicted, such that the Poisson's ratio used here was 0.3. The ϵ is the lattice mismatch degree, which was calculated using $\epsilon = 2/3 \cdot \Delta a/a$ [49]. The lattice constant of the precipitated phase and matrix was derived from XRD results. The r and f were the precipitated phase radius and volume fraction and derived from TEM photos; b the Burgers vector, derived using $b = \sqrt{3}/2a$; a the lattice constant of the matrix; and m a constant, at 0.85 [50]. Based on the relevant literature [51,52], the shear modulus of AlZr_3 was 55.14 GPa and the reversed-phase domain boundary energy (γ_{app}) of Al-Zr alloy 0.447 J/m². The relevant parameters of precipitation strengthening are listed in Table 5 and calculated contribution values of each strengthening listed in Table 6. As $\Delta\sigma_{CS} + \Delta\sigma_{MS}$ of $\text{Al}_{0.1}$ or $\text{Al}_{0.5}$ was greater than $\Delta\sigma_{OS}$, the precipitation strengthening effect was considered to be dominated by coherent strengthening and modulus strengthening.

Finally, the yield strength calculation and experimental results as well as the proportion of each strength contribution were examined (Fig. 12). The yield strength calculation results were very close to the experimental results. However, as the solution strengthening model did not consider thermal activation effects, there were still some discrepancies between predicted values and experimental measurements. In the absence of Al, the strengthening effect in the alloy

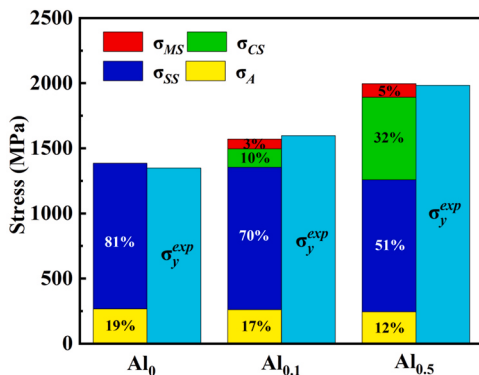


Fig. 12. Calculation and experiment yield stress values of the $\text{Al}_x(\text{TiZrTa}_{0.7}\text{NbMo})$ alloys.

was largely attributable to solution strengthening, whose contribution reached 81 %, which coincided with the characteristics of high solution strengthening of high entropy alloys. When 0.1 mol of Al was added, solution strengthening was still the major contribution, but the proportion of solution strengthening contribution decreased as the result of the precipitation strengthening effect. With increased Al, the contribution of precipitation strengthening increased. When the Al content reached 0.5 mol, the contribution degree of precipitation strengthening increased to 37 % and the difference with the contribution degree of the solution strengthening only 14 %. After Al addition, solution strengthening gradually decreased, indicating that the addition of Al element reduced the degree of alloy lattice distortion (Table 6). Among the three effects of precipitation strengthening, the contribution of coherence strengthening had the highest proportion, indicating that the precipitation strengthening effect was primarily attributable to the mismatch factor between the AlZr_3 phase and matrix lattice constant. This suggested that lattice distortion occurred around AlZr_3 particles, thus forming a certain stress field and further increasing the alloy yield strength.

4.3. High temperature mechanical properties

The effects of Al content on the yield strength of the alloy at compression temperatures of 800, 1000, and 1200 °C were examined (Fig. 13). In $\text{TiZrTa}_{0.7}\text{Nb}$ alloy, because Al was not added, only the solution strengthening mechanism was present in the alloy. When the temperature increased from 800 to 1000 and 1200 °C in sequence, the yield strength decreased by 176 and 229 MPa,

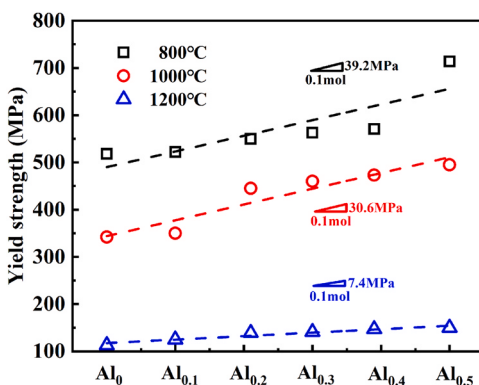


Fig. 13. Dependence of the yield stress on the mole of Al in $\text{Al}_x(\text{TiZrTa}_{0.7}\text{NbMo})$ alloys at 800, 1000, and 1200 °C.

respectively. The temperature rise thus clearly decreased the contribution degree of solution strengthening. The current research has indicated that, when the temperature was higher than 600 °C, dislocations in the alloy prone to movement, which reduced its yield strength. In addition, as the temperature increases, dislocation movements were more likely to occur [53]. Also, during high-temperature compression, the redistribution of elements at grain boundaries could have effectively reduced elastic lattice distortion arising from the atomic radius differences in the alloy, thereby reducing the solution strengthening effect.

With Al₀ as the initial matrix, after the addition of different Al proportions, the part contributing to the decrease of solution strengthening contribution caused by Al addition was ignored here. Therefore, the increase in yield strength was attributed entirely to the effect of precipitation strengthening. At the compression temperatures of 800, 1000, and 1200 °C, the yield strength of the alloy increased by 39.2, 30.6, and 7.4 MPa, respectively, for each 0.1 mol increase in Al content (Fig. 13). The increase in Al content clearly effectively increased the yield strength of the alloy, while increased temperature reduced the precipitation strengthening effect. The increase in yield strength due to increased Al content might have been associated with increased volume fraction of the precipitated phase. At high temperatures, grain boundary slip is the major deformation mechanism [43]. Hence, when the temperature is insufficient to completely dissolve the precipitated phases, hard, fine, and dispersed precipitated phases in the alloy helped fix the grain boundaries [54], thus increasing the slip resistance of the dislocation and hindering dislocation migration. In addition, temperatures had a significant impact on the strengthening effect of the precipitated phase. After adding Al, the improvement of the alloy yield strength was significantly less than that at 800 vs. 1200 °C. This was because, as the temperature rise, the solute solubility within the alloy was increasing and the precipitated phase also dissolved in the matrix in small amounts. This increased the density of movable dislocations in the alloy, ultimately leading to decreased stress [55]. A higher deformation temperature will lead to weaker precipitation strengthening effects. When the temperature rose to a certain extent, the precipitation enhancement will thoroughly fail. Therefore, the improvement of the yield strength of the material here was not significant at 1200 °C.

4.4. Mechanical property comparison of RHEAs

The $\text{Al}_x(\text{TiZrTa}_{0.7}\text{NbMo})$ series alloys prepared here were compared with some existing Al-containing refractory high-entropy alloys [17,20,56–60] regarding room temperature and high temperature mechanical properties. A comparison diagram of the yield strength of the alloy at different temperatures and the relationship between yield strength and plastic strain of the alloy at room temperature are shown in Fig. 14a and 14b. Also, $\text{Al}_x(\text{TiZrTa}_{0.7}\text{NbMo})$ alloys still had a yield strength of 400–500 MPa at high temperatures. However, the precipitated phase formed as a result of Al addition usually severely jeopardizes the room temperature plasticity and the room temperature fracture strain of most Al-containing refractory high-entropy alloys did not exceed 5 % (Fig. 14b). The room temperature plasticity of this alloy series was greater than that of most existing Al-containing refractory high-entropy alloys. For example, Al_{0.2} alloy still had a plastic strain of 27.9 % when its yield strength was 1651 MPa. The comparison indicated that $\text{Al}_x(\text{TiZrTa}_{0.7}\text{NbMo})$ alloy had excellent high temperature and room temperature mechanical properties, demonstrating the potential to become a high temperature material with good comprehensive mechanical properties.

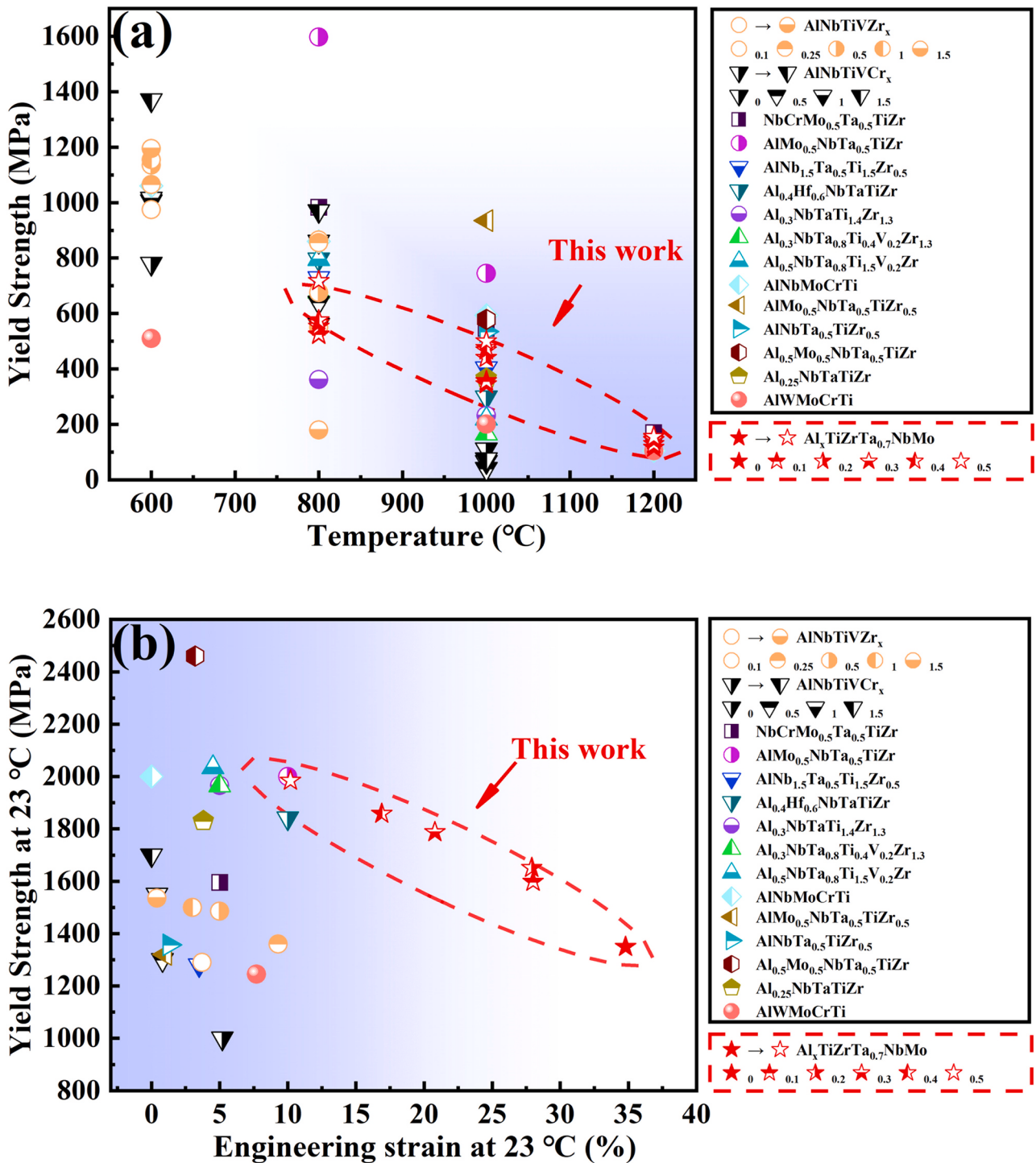


Fig. 14. Temperature dependence of the yield strength of $\text{Al}_x(\text{TiZrTa}_{0.7}\text{NbMo})$ RHEAs and some RHEAs (a) and the relationship between yield strength of $\text{Al}_x(\text{TiZrTa}_{0.7}\text{NbMo})$ RHEAs and some RHEAs and plasticity at 23 °C (b).

5. Conclusions

To further study and develop refractory high-entropy alloys as a high-temperature material, $\text{Al}_x(\text{TiZrTa}_{0.7}\text{NbMo})$ ($x = 0, 0.1, 0.2, 0.3, 0.4, 0.5$) series alloys were prepared by vacuum arc melting method and annealed at 1000 °C for 12 h. The effects of Al addition on the phase composition, microstructures, and room and high temperature compressive mechanical properties of the alloys were systematically examined. The following conclusions were drawn:

(1) After annealing at 1000 °C, the structure of $\text{Al}_x(\text{TiZrTa}_{0.7}\text{NbMo})$ alloy comprised BCC₁ and BCC₂ phases, which corresponded to branch and intergranular regions in the microstructure, respectively. Ta, Nb, and Mo were enriched in BCC₁ phase and Ti, Zr, and Al elements enriched in BCC₂ phase. With increased Al content, the AlZr₃ phase of L1₂ metal compound were precipitated between dendrites.

(2) The thermodynamic model of $\text{Al}_x(\text{TiZrTa}_{0.7}\text{NbMo})$ alloys showed that the alloy will develop a double-phase structure after

solidification. At higher Al content, compounds of AlZr_2 and Al_2Zr_3 were formed. The thermodynamic model successfully predicted that the alloys contained BCC_1 and BCC_2 phases. However, only the AlZr_2 phase detected in the alloy as a result of annealing treatment.

(3) After Al addition, the room temperature yield strength of the alloys increased from 1349 to 1984 MPa, while the plastic strain decreased from 34.8 % to 10.2 %. The analysis of mechanical strengthening model showed that, when Al was not added, the alloy strengthening mechanism was dominated by solution strengthening, which accounts for 81 %. After adding 0.1–0.5 mol of Al, the contribution of precipitation strengthening gradually increased from 13 % to 37 %. The precipitation strengthening effect was attributable to the combination of coherent strengthening and modulus strengthening.

(4) At high temperatures, the yield strength of $\text{Al}_x(\text{TiZrTa}_{0.7}\text{NbMo})$ alloys improved with increased Al. At 800, 1000, and 1200 °C, addition of 0.1 mol in Al content improved the yield strength by 39.2, 30.6, and 7.4 MPa, respectively.

RediT authorship contribution statement

Fuyu Dong and Yue Zhang: Resources, Conceptualization, Methodology, Writing-Review & Editing. Zihua Guo and Jinyuan Guan: Formal analysis, Data Curation, Writing-Original Draft. Xiangyang Shen and Feng Liu: Investigation. Yinxiao Wang and Binbin Wang: Investigation. Liangshun Luo and Jun Cheng: Investigation. Yinxiao Wang: Resources, Project administration. Xiaoguang Yuan and Yanqing Su: Visualization, Project administration, Validation.

Data availability

Data will be made available on request.

Declaration of Competing Interest

We declare that we have no financial and personal relationships with other people or organizations that can inappropriately influence our work, there is no professional or other personal interest of any nature or kind in any product, service and/or company that could be construed as influencing the position presented in, or the review of, the manuscript entitled "Microstructure and mechanical properties of $\text{Al}_x(\text{TiZrTa}_{0.7}\text{NbMo})$ refractory high-entropy alloys".

Acknowledgments

The present work was supported by National Natural Science Foundation of China (No. 52101037 and 52271249), Natural Science Foundation of Liaoning Province (No. 2021-KF-15-01), The Grant Plan for Young and Middle-aged Innovation Scientists of Shenyang Government (No. RC210058), Basic Scientific Research Project of Education Department of Liaoning Province (No. LJKMZ20220466), and Key Research and Development Program of Shaanxi (No. 2023-YBGY-488).

References

- [1] K. Lu, Materials science. The future of metals, *Science* 328 (5976) (2010) 319–320.
- [2] D. Gu, X. Shi, R. Poprawe, D.L. Bourell, R. Setchi, J. Zhu, Material-structure-performance integrated laser-metal additive manufacturing, *Science* 372 (6545) (2021).
- [3] J.H. Perepezko, Materials science. The hotter the engine, the better, *Science* 326 (5956) (2009) 1068–1069.
- [4] J.-W. Yeh, S.-K. Chen, S.-J. Lin, J.-Y. Gan, T.-S. Chin, Nanostructured high-entropy alloys with multiple principal elements: novel alloy design concepts and outcomes, *Adv. Eng. Mater.* 6 (5) (2004) 299–303.
- [5] B. Cantor, I.T.H. Chang, P. Knight, A.J.B. Vincent, Microstructural development in equiatomic multicomponent alloys, *Mater. Sci. Eng.: A* 375–377 (2004) 213–218.
- [6] S. Wu, D. Qiao, H. Zhang, J. Miao, H. Zhao, J. Wang, Y. Lu, T. Wang, T. Li, Microstructure and mechanical properties of CxHf0.25NbTaW0.5 refractory high-entropy alloys at room and high temperatures, *J. Mater. Sci. Technol.* 97 (2022) 229–238.
- [7] B. Chai, J. Xiong, Z. Guo, J. Liu, L. Ni, Y. Xiao, C. Chen, Structure and high temperature wear characteristics of CVD coating on HEA-bonded cermet, *Ceram. Int.* 45 (15) (2019) 19077–19085.
- [8] A. Raza, S. Abdulahad, B. Kang, H.J. Ryu, S.H. Hong, Corrosion resistance of weight reduced AlxCrFeMoV high entropy alloys, *Appl. Surf. Sci.* 485 (2019) 368–374.
- [9] O.N. Senkov, G.B. Wilks, D.B. Miracle, C.P. Chuang, P.K. Liaw, Refractory high-entropy alloys, *Intermetallics* 18 (9) (2010) 1758–1765.
- [10] O.N. Senkov, G.B. Wilks, J.M. Scott, D.B. Miracle, Mechanical properties of Nb25Mo25Ta25W25 and $\text{V20Nb20Mo20Ta20W20}$ refractory high entropy alloys, *Intermetallics* 19 (5) (2011) 698–706.
- [11] K. Gao, J.Z. Wang, Y.H. Meng, Y. Li, Y. Zhang, Phase stability and compressive properties of low-density $(\text{Zr50Ti35Nb15})_{100-x}\text{Al}_x$ high entropy alloys, *Intermetallics* 148 (2022).
- [12] N. Yurchenko, E. Panina, M. Tikhonovsky, G. Salishchev, S. Zhrebtssov, N. Stepanov, Structure and mechanical properties of an *in situ* refractory $\text{Al20Cr10Nb15Ti20V25Zr10}$ high entropy alloy composite, *Mater. Lett.* 264 (2020).
- [13] O. Senkov, D. Isheim, D. Seidman, A. Pilchak, Development of a refractory high entropy superalloy, *Entropy* 18 (3) (2016) 102–115.
- [14] N.N. Guo, L. Wang, L.S. Luo, X.Z. Li, R.R. Chen, Y.Q. Su, J.J. Guo, H.Z. Fu, Microstructure and mechanical properties of refractory high entropy $(\text{Mo}0.5\text{NbHf0.5ZrTi})(\text{BCC})/\text{M5Si3}$ *in-situ* compound, *J. Alloy. Compd.: Interdiscip. J. Mater. Sci. Solid-State Chem. Phys.* (660) (2016) 197–203.
- [15] O.N. Senkov, S.V. Senkova, C. Woodward, Effect of aluminum on the microstructure and properties of two refractory high-entropy alloys, *Acta Mater.* 68 (2014) 214–228.
- [16] D. Qiao, H. Liang, S. Wu, J. He, Z. Cao, Y. Lu, T. Li, The mechanical and oxidation properties of novel B2-ordered $\text{Ti2ZrHf0.5VNb0.5Al}_x$ refractory high-entropy alloys, *Mater. Charact.* 178 (2021).
- [17] O.N. Senkov, C. Woodward, D.B. Miracle, Microstructure and properties of aluminum-containing refractory high-entropy alloys, *Jom* 66 (10) (2014) 2030–2042.
- [18] V. Soni, B. Gwalani, T. Alam, S. Dasari, Y. Zheng, O.N. Senkov, D. Miracle, R. Banerjee, Phase inversion in a two-phase, BCC+B2, refractory high entropy alloy, *Acta Mater.* 185 (2020) 89–97.
- [19] C.-M. Lin, C.-C. Juan, C.-H. Chang, C.-W. Tsai, J.-W. Yeh, Effect of Al addition on mechanical properties and microstructure of refractory AlxHfNbTaTiZr alloys, *J. Alloy. Compd.* 624 (2015) 100–107.
- [20] O.N. Senkov, J.K. Jensen, A.L. Pilchak, D.B. Miracle, H.L. Fraser, Compositional variation effects on the microstructure and properties of a refractory high-entropy superalloy $\text{AlMo0.5NbTa0.5TiZr}$, *Mater. Des.* 139 (2018) 498–511.
- [21] D.B. Miracle, M.-H. Tsai, O.N. Senkov, V. Soni, R. Banerjee, Refractory high entropy superalloys (RSAs), *Scr. Mater.* 187 (2020) 445–452.
- [22] A. Takeuchi, A. Inoue, Classification of bulk metallic glasses by atomic size difference, heat of mixing and period of constituent elements and its application to characterization of the main alloying element, *Mater. Trans.* 46 (12) (2005) 2817–2829.
- [23] T.B. Massalski, H. Okamoto, P. Subramanian, et al., *Binary alloy phase diagrams*, ASM International, OH, 1990.
- [24] S. Ge, H. Fu, L. Zhang, H. Mao, H. Li, A. Wang, W. Li, H. Zhang, Effects of Al addition on the microstructures and properties of MoNbTaTiV refractory high entropy alloy, *Mater. Sci. Eng.: A* 784 (2020).
- [25] W. Zheng, S. Lü, S. Wu, X. Chen, W. Guo, Development of MoNbVTax refractory high entropy alloy with high strength at elevated temperature, *Mater. Sci. Eng.: A* 850 (2022).
- [26] S. Guo, C. Ng, J. Lu, C.T. Liu, Effect of valence electron concentration on stability of fcc or bcc phase in high entropy alloys, *J. Appl. Phys.* 109 (10) (2011).
- [27] X. Yang, Y. Zhang, Prediction of high-entropy stabilized solid-solution in multi-component alloys - ScienceDirect, *Mater. Chem. Phys.* 132 (2–3) (2012) 233–238.
- [28] O.N. Senkov, D.B. Miracle, K.J. Chaput, J.-P. Couzinie, Development and exploration of refractory high entropy alloys—A review, *J. Mater. Res.* 33 (19) (2018) 3092–3128.
- [29] Y. Iijima, T. Nagase, A. Matsugaki, et al., Design and development of Ti-Zr-Hf-Nb-Ta-Mo high-entropy alloys for metallic biomaterials, *Mater. Des.* 202 (1) (2021) 109548.
- [30] S.-P. Wang, E. Ma, J. Xu, New ternary equi-atomic refractory medium-entropy alloys with tensile ductility: Hafnium versus titanium into NbTa-based solution, *Intermetallics* 107 (2019) 15–23.
- [31] J. Yang, J.W. Qiao, S.G. Ma, G.Y. Wu, D. Zhao, Z.H. Wang, Revealing the Hall-Petch relationship of Al0.1CoCrFeNi high-entropy alloy and its deformation mechanisms, *J. Alloy. Compd.* 795 (2019) 269–274.
- [32] Y. Gao, High Entropy Alloys: Solid Solution Strengthening, in: F.G. Caballero (Ed.), *Encyclopedia of Materials: Metals and Alloys*, Elsevier, Oxford, 2022, pp. 435–440.
- [33] O.N. Senkov, S.L. Semiatin, Microstructure and properties of a refractory high-entropy alloy after cold working, *J. Alloy. Compd.* 649 (2015) 1110–1123.
- [34] S.P. Wang, J. Xu, TiZrNbTaMo high-entropy alloy designed for orthopedic implants: As-cast microstructure and mechanical properties, *Mater. Sci. Eng. C. Mater. Biol. Appl.* 73 (2017) 80–89.

- [35] X. Yan, P.K. Liaw, Y. Zhang, Ultrastrong and ductile BCC high-entropy alloys with low-density via dislocation regulation and nanoprecipitates, *J. Mater. Sci. Technol.* 110 (2022) 109–116.
- [36] T. Li, S. Wang, W. Fan, Y. Lu, T. Wang, T. Li, P.K. Liaw, CALPHAD-aided design for superior thermal stability and mechanical behavior in a TiZrHfNb refractory high-entropy alloy, *Acta Mater.* 246 (2023).
- [37] B.H. Chen, S.G. Liu, P.F. Ji, B. Li, X.Y. Zhang, M.Z. Ma, R.P. Liu, Investigation on microstructure and mechanical properties of multiphase ZrSn1.5Alx alloy with simultaneous enhancement of strength and plasticity, *J. Alloy. Compd.* 831 (2020).
- [38] R. Labusch, Statistische theoreien der mischkristallh??rtung, *Acta Metall.* 20 (7) (1972) 917–927.
- [39] S.-P. Wang, J. Xu, TiZrNbTa)-Mo high-entropy alloys: dependence of microstructure and mechanical properties on Mo concentration and modeling of solid solution strengthening, *Intermetallics* 95 (2018) 59–72.
- [40] I. Toda-Caraballo, P.E.J. Rivera-Díaz-del-Castillo, Modelling solid solution hardening in high entropy alloys, *Acta Mater.* 85 (2015) 14–23.
- [41] O.N. Senkov, J.M. Scott, S.V. Senkova, D.B. Miracle, C.F. Woodward, Microstructure and room temperature properties of a high-entropy TaNbHfZrTi alloy, *J. Alloy. Compd.* 509 (20) (2011) 6043–6048.
- [42] S. Zeng, Y. Zhou, H. Li, H. Zhang, H. Zhang, Z. Zhu, Microstructure and mechanical properties of lightweight Ti3Zr1.5NbVAl ($x = 0, 0.25, 0.5$ and 0.75) refractory complex concentrated alloys, *J. Mater. Sci. Technol.* 130 (2022) 64–74.
- [43] Y. Cao, W. Zhang, B. Liu, Y. Liu, M. Du, A. Fu, Phase decomposition behavior and its effects on mechanical properties of TiNbTa0.5ZrAl0.5 refractory high entropy alloy, *J. Mater. Sci. Technol.* 66 (2021) 10–20.
- [44] C. Booth-Morrison, D.C. Dunand, D.N. Seidman, Coarsening resistance at 400 °C of precipitation-strengthened Al-Zr-Sc-Er alloys, *Acta Mater.* 59 (18) (2011) 7029–7042.
- [45] D.N. Seidman, E.A. Marquis, D.C. Dunand, Precipitation strengthening at ambient and elevated temperatures of heat-treatable Al(Sc) alloys, *Acta Mater.* 50 (16) (2002) 4021–4035.
- [46] H. Wen, T.D. Topping, D. Isheim, D.N. Seidman, E.J. Lavernia, Strengthening mechanisms in a high-strength bulk nanostructured Cu-Zn-Al alloy processed via cryomilling and spark plasma sintering, *Acta Mater.* 61 (8) (2013) 2769–2782.
- [47] K. Ma, H. Wen, T. Hu, T.D. Topping, D. Isheim, D.N. Seidman, E.J. Lavernia, J.M. Schoenung, Mechanical behavior and strengthening mechanisms in ultra-fine grain precipitation-strengthened aluminum alloy, *Acta Mater.* 62 (2014) 141–155.
- [48] J. Bo, A. Melander, On the critical resolved shear stress from misfitting particles, *Scr. Metall.* 12 (6) (1978) 497–498.
- [49] J.Y. He, H. Wang, H.L. Huang, X.D. Xu, M.W. Chen, Y. Wu, X.J. Liu, T.G. Nieh, K. An, Z.P. Lu, A precipitation-hardened high-entropy alloy with outstanding tensile properties, *Acta Mater.* 102 (2016) 187–196.
- [50] C. Li, Y. Ma, J. Hao, Y. Yan, Q. Wang, C. Dong, P.K. Liaw, Microstructures and mechanical properties of body-centered-cubic (Al,Ti)0.7(Ni,Co,Fe,Cr)5 high entropy alloys with coherent B2/L21 nanoprecipitation, *Mater. Sci. Eng.: A* 737 (2018) 286–296.
- [51] L. Wang, S. Hou, D. Liang, First-principles investigations on the phase stability, elastic and thermodynamic properties of Zr-Al alloys, *Int. J. Mod. Phys. C* 26 (12) (2015).
- [52] L. Ding, M. Zhao, Z. Jia, Y. Weng, K. Xiang, X. Wu, Q. Liu, On the formation of anti-phase boundaries and interphase boundaries in Al3Zr precipitates of Al-Cu-Zr alloy studied at atomic scale, *J. Alloy. Compd.* 887 (2021).
- [53] O.N. Senkov, S.J. Kuhr, J.M. Shank, E.J. Payton, C. Woodward, Microstructure and properties of an equiatomic TaTiZr alloy, *Mater. Sci. Eng.: A* 814 (2021).
- [54] L. Han, X. Xu, L. Wang, F. Pyczak, R. Zhou, Y. Liu, A eutectic high-entropy alloy with good high-temperature strength-plasticity balance, *7* (11) (2019) 460–466.
- [55] O.N. Senkov, J.P. Couzinie, S.I. Rao, V. Soni, R. Banerjee, Temperature dependent deformation behavior and strengthening mechanisms in a low density refractory high entropy alloy Al10Nb15Ta5Ti30Zr40, *Materialia* 9 (2020).
- [56] O.N. Senkov, C.F. Woodward, Microstructure and properties of a refractory NbCrMo0.5Ta0.5TiZr alloy, *Mater. Sci. Eng.: A* 529 (2011) 311–320.
- [57] N.D. Stepanov, N.Y. Yurchenko, D.V. Skibin, M.A. Tikhonovsky, G.A. Salishchev, Structure and mechanical properties of the AlCr_xNbTiV ($x = 0, 0.5, 1, 1.5$) high entropy alloys, *J. Alloy. Compd.* 652 (2015) 266–280.
- [58] H. Chen, A. Kauffmann, B. Gorr, D. Schliephake, C. Seemüller, J.N. Wagner, H.J. Christ, M. Heilmayer, Microstructure and mechanical properties at elevated temperatures of a new Al-containing refractory high-entropy alloy Nb-Mo-Cr-Ti-Al, *J. Alloy. Compd.* 661 (2016) 206–215.
- [59] N.Y. Yurchenko, N.D. Stepanov, S.V. Zherebtsov, M.A. Tikhonovsky, G.A. Salishchev, Structure and mechanical properties of B2 ordered refractory AlNbTiVZr ($x = 0-1.5$) high-entropy alloys, *Mater. Sci. Eng.: A* 704 (2017) 82–90.
- [60] H. Naser-Zoshki, A.-R. Kiani-Rashid, J. Vahdati-Khaki, Design of a low density refractory high entropy alloy in non-equiautomic W-Mo-Cr-Ti-Al system, *Vacuum* 181 (2020).